ADVANCED FUNCTIONAL MATERIALS
www.afm-journal.de

DNA Sensing Using Nanocrystalline Surface-Enhanced Al_2O_3 Nanopore Sensors

By *Bala Murali Venkatesan, Amish B. Shah, Jian-Min Zuo,* and *Rashid Bashir**

A new solid-state, Al_2O_3 nanopore sensor with enhanced surface properties for the real-time detection and analysis of individual DNA molecules is reported. Nanopore formation using electron-beam-based decomposition transforms the local nanostructure and morphology of the pore from an amorphous, stoichiometric structure (O to Al ratio of 1.5) to a heterophase crystalline network, deficient in O (O to Al ratio of ≈0.6). Direct metallization of the pore region is observed during irradiation, thereby permitting the potential fabrication of nanoscale metallic contacts in the pore region with application to nanopore-based DNA sequencing. Dose-dependent phase transformations to purely γ and/or α-phase nanocrystallites are also observed during pore formation, allowing for surface-charge engineering at the nanopore/fluid interface. DNA transport studies reveal an order-of-magnitude reduction in translocation velocities relative to alternate solid-state architectures, accredited to high surface-charge density and the nucleation of charged nanocrystalline domains. The unique surface properties of Al_2O_3 nanopore sensors make them ideal for the detection and analysis of single-stranded DNA, double-stranded DNA, RNA secondary structures, and small proteins. These nanoscale sensors may also serve as useful tools in studying the mechanisms driving biological processes including DNA–protein interactions and enzyme activity at the single-molecule level.

1. Introduction

Solid-state nanopores-based technologies are emerging as next-generation bionanosensors for the electrical detection, analysis, and manipulation of single biomolecules, particularly DNA, RNA, and small proteins, applicable to DNA sequencing. The electrical detection of target molecules through these solid-state pores is typically measured using two-terminal electrophoresis, resulting in characteristic blockades in the measured ionic current. This technique has been used for rapid, label-free nucleic acid-based detection of single-nucleotide polymorphisms (SNPs) affecting gene expression,[1] detection of DNA methylation with application to cancer diagnostics,[2] DNA sizing and sieving,[3] and detection of DNA–protein complexes essential for homologous recombination and DNA repair.[4] In addition, nanopores show tremendous potential as high-throughput, cost-effective DNA sequencing platforms with the sensitivity and specificity needed for sequence identification without prior DNA modification, fluorescent labeling, or polymer chain reaction (PCR) amplification. Proteinaceous mutant α-hemolysin nanopores are currently capable of identifying individual bases, making way for a sequencing-by-exonuclease-digestion-based approach.[5] The utility of biological nanopores as commercial diagnostic tools, however, is hindered by their limited lifetime, low dynamic voltage range (beyond which electrical breakdown of the supporting lipid bilayer occurs) and their lack of mechanical stability.[6] In contrast, solid-state nanopores are functional over a wider range of temperatures, voltages, and solvent conditions and can be tuned in diameter with subnanometer precision.[7–9] In addition, they allow for potential device integration with lateral sensing electrodes and lab-on-a-chip technologies.

Solid-state nanopores are typically formed through ion-beam sculpting or electron-beam-based sputtering/oxide re-flow processes in thin Si_3N_4 or SiO_2 membranes.[7–9] More recently, we demonstrated the fabrication of highly sensitive, mechanically stable nanopore sensors in Al_2O_3 membranes formed via electron-beam-based decompositional sputtering processes.[10] These pores were mechanically more robust than their SiO_2 counterparts, exhibited state-of-the-art noise performance and allowed for true very-large-scale integration (VLSI) and device-level

[*] Prof. R. Bashir, B. M. Venkatesan
Department of Electrical and Computer Engineering
University of Illinois at Urbana Champaign
Urbana, IL 61801 (USA)
E-mail: rbashir@illinois.edu
Prof. R. Bashir, B. M. Venkatesan
Micro and Nanotechnology Laboratory
University of Illinois at Urbana Champaign
Urbana, IL 61801 (USA)
Prof. R. Bashir, A. B. Shah, Prof. J. M. Zuo
Frederick Seitz Materials Research Laboratory
University of Illinois at Urbana Champaign
Urbana, IL 61801 (USA)
Prof. R. Bashir
Department of Bioengineering
University of Illinois at Urbana Champaign
Urbana, IL 61801 (USA)
A. B. Shah, Prof. J. M. Zuo
Department of Materials Science and Engineering
University of Illinois at Urbana Champaign
Urbana, IL 61801 (USA)

DOI: 10.1002/adfm.200902128

integration due to the rapid, low-temperature fabrication process developed using atomic layer deposition (ALD). The application of such technologies to widespread nucleic acid-based diagnostics, however, requires further insight into the material-dependent mechanisms driving the pore formation process and subsequent interactions between DNA and the nanopore.

In this Full Paper, we discuss the impact of material selection on the kinetics of DNA transport and present a qualitative model describing the nanopore formation process in Al_2O_3. Drastic changes in the material properties of the nanopore were observed during its nucleation and expansion, significantly impacting the sensitivity of these nanoscale single-molecule sensors. Prolonged electron-beam irradiation resulted in changes in the local stoichiometry and morphology of the pore from an amorphous, stoichiometric structure (O to Al ratio of 1.5 as expected in stoichiometric Al_2O_3) to a heterophase, crystalline structure with a non-stoichiometric O to Al ratio of ≈0.6. Preferential phase transformations from γ-, α-, κ-, and δ-Al_2O_3 nanocystallites to purely γ- and α-phases were observed with increasing electron dose. Precise control over phase transformations in Al_2O_3 systems by varying electron dose provides a rudimentary method to engineer surface charge at the nanopore/fluid interface. Direct metallization of the irradiated region was also observed with prolonged electron-beam exposure, attributed to the preferential desorption of O and the aggregation of metallic Al clusters as confirmed through nanoarea electron diffraction (NED) and electron energy loss spectroscopy (EELS) in the transmission electron microscopy (TEM) system. This in-situ metallization process can possibly be used to fabricate a single nanoscale metallic contact directly in the nanopore. An applied potential to this contact would allow the direct manipulation of localized electric-field gradients, thereby affecting surface charge and pore conductivity, perhaps even enabling the electrostatic capture of charged biomolecules in the nanopore. The translocation of dsDNA through these *nanometer*-sized alumina pores revealed average translocation velocities that were an order of magnitude less than that observed in Si_3N_4 and SiO_2 systems under similar conditions, attributed to strong DNA–nanopore interactions. At present, high DNA translocation velocities (≈30 bases/μs)[6] limit the utility of conventional SiO_2 and Si_3N_4-based nanopore technologies in high-end DNA sensing and analysis applications, including single-nucleotide detection. In addition, the detection of these fast translocation events requires high-bandwidth measurements, which in turn reduces the signal-to-noise ratio in DNA detection experiments. Thus, a nanopore architecture with an intrinsic ability to interact with DNA to reduce biomolecule transport velocities is highly desirable. Electron-beam-irradiated Al_2O_3 nanopore sensors provide such a capability. Two distinct polymer–pore interaction mechanisms influenced DNA translocation kinetics: electrostatic binding of anionic DNA to the positively charged nanopore surface enhanced by γ- and α-Al_2O_3 nanocrystallite formation and hydrophobic polymer–pore interactions promoted by the relatively high surface roughness of electron-beam-irradiated Al_2O_3. Our results confirm that nanopores formed in metal oxide systems indeed provide a viable and highly functional alternative to conventional nanopore sensors, serving as effective tools for high-throughput single-molecule DNA analysis.

2. Results and Discussion

2.1. Device Characterization and Overview

The solid-state nanopore fabrication process used herein builds on prior work.[10] Low-stress, mechanically stable 45 ± 5-nm-thick amorphous Al_2O_3 membranes were formed using standard microfabrication processes, as described in the Experimental Section. The inset of Figure 1a is a cross sectional TEM image of a ≈40-nm membrane post release (Region 3). Metal was sputtered on both sides of the membrane during TEM sample preparation, as shown by regions 1, 2, 4, and 5 for stability during cross sectioning. Energy dispersive X-ray spectroscopy (EDS) confirmed that the membrane contained only Al and O, as shown in Figure 1a. Nanopores of varying diameter were formed in these free-standing amorphous Al_2O_3 membranes using a focused electron beam from a JEOL JEM2010F field-emission TEM operated at 197 kV. Figure 1b is a TEM image of a 7-nm nanopore formed using this process. The shot noise in the pore region confirms that the electron beam has completely sputtered through the membrane. The pore quenches in size and retains its shape upon removal of the electron beam. This technique thereby allows for precise tunability and nanometer control over pore dimensions. Post fabrication, nanopore chips were O_2 plasma treated and immediately mounted between two compartments of a Delrin flow cell into which 1 M KCl with 10 mM Tris-HCl pH 7.5 was introduced. Current through the nanopore was measured by placing Ag/AgCl electrodes in each reservoir, with the nanopore forming the only electrical/fluidic connection between the two compartments. Immediate wetting and ionic conduction through the pore was observed. In addition, linear current–voltage (*IV*) characteristics at different electrolyte concentrations (1 M, 100 mM, and 10 mM) were observed for all pores measured, suggesting a symmetric nanopore structure. The linear *IV* characteristics of a 5-nm pore in 1 M, 100 mM, and 10 mM KCl electrolyte are shown in Figure 1c. The three-dimensional (3D) geometry of the pore was extracted through a series of conductance measurements and energy-filtered TEM and was confirmed to be a symmetric, double-cone structure.[10] Figure 1d is a schematic representation of DNA translocation through a nanopore under an applied bias. DNA translocation studies involved the use of 5 kbp dsDNA (NoLimits) from Fermantas Inc. with double-stranded DNA (dsDNA) being inserted into the chamber containing the anode (negative terminal) at a final concentration of 6 nM in 100 mM KCl, 10 mM Tris-HCl, pH 7.5 electrolyte. Prior to the introduction of dsDNA, steady, blockade-free open-pore currents were observed, as shown in the inset of Figure 1e. After DNA insertion, characteristic current blockades/translocation events were seen, as shown in Figure 1e.

2.2. Nanopore Nucleation

Focused electron probes in the TEM with diameters of 2.3 nm, 2.7 nm, 3.2 nm, and 3.9 nm full width at half-maximum (FWHM) corresponding to beam current densities of 2.6×10^6 A m^{-2}, 4.2×10^6 A m^{-2}, 6.1×10^6 A m^{-2}, and 1.2×10^7 A m^{-2}, respectively, were used to sputter nanopores of varying diameter. The sputtering process in Al_2O_3 is attributed to the Coulomb explosion displacement of atoms based on the Knotek–Feibelman electron-stimulated

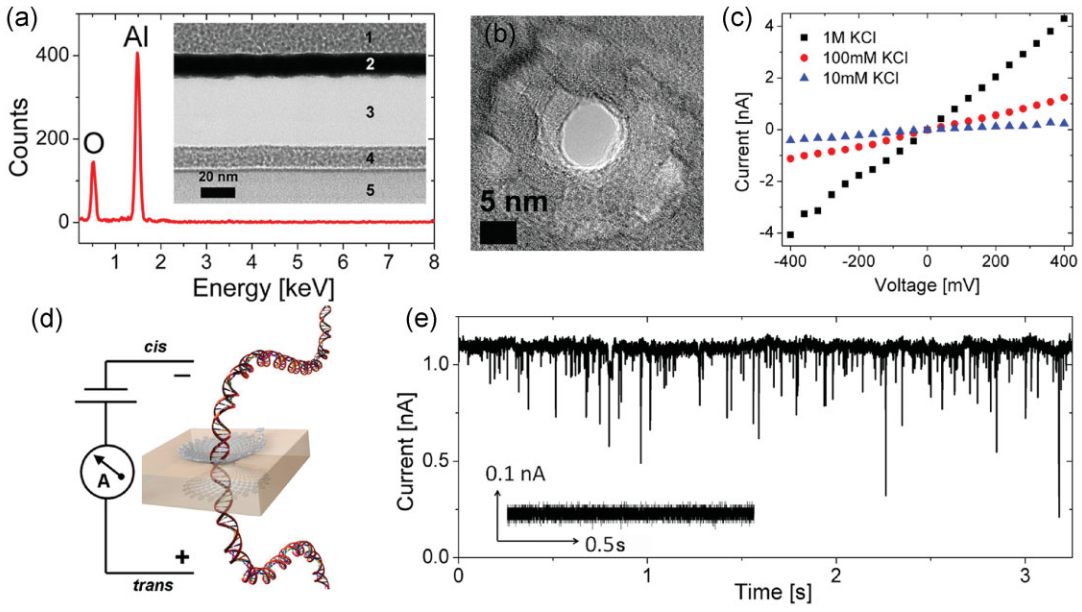

Figure 1. a) EDS spectrum from an Al_2O_3 membrane confirming the presence of only Al and O. Inset) TEM cross section of 40-nm-thick Al_2O_3 membrane (Region 3) in which nanopores were formed. b) TEM phase-contrast image of a 7-nm pore formed using a focused convergent electron beam. c) Linear *IV* characteristics from a ~5-nm Al_2O_3 nanopore at KCl concentrations of 10 mM, 100 mM, and 1 M. d) Schematic image of DNA transport through a nanopore under an applied bias. e) Characteristic current blockades observed during DNA translocation of 5 kbp dsDNA through 7-nm pore at 500 mV. Inset) Control prior to the insertion of dsDNA shows steady, blockade-free current.

desorption mechanism.[12] The generation of positively charged oxygen ions results in a repulsive lattice potential forcing O^+ ions to either desorb from the surface (surface dissociated mechanisms) or to move to interstitial sites, thereby creating Frenkel pairs within the bulk of the material (volume dissociated mechanisms). This decompositional sputtering process was used to form nanopores ranging in diameter from 2 to 30 nm. The intensity profiles of the various electron probes used in these experiments are illustrated in Figure 2a, normalized with respect to the maximum peak intensity of the 3.9 nm probe. The inset of Figure 2a is a TEM image of a 3.2-nm probe, light areas indicating regions of maximum electron intensity located at the center of the probe and darker areas indicating less intense regions located in the tail of the probe. Comparative probe analysis revealed that larger probe sizes exhibited higher peak intensities and a broader Gaussian–Lorentzian profile and were more suited for forming larger nanopores with diameters in the range of 10–30 nm. Such platforms are applicable for single-molecule protein analysis and the detection of large analytes. In contrast, smaller probes (2.7 nm and 3.2 nm) exhibited lower peak intensity and a narrower profile, ideal for the high-precision fabrication of 2–10-nm pores in Al_2O_3. These structures were well suited for single-stranded DNA (ssDNA), dsDNA, and RNA single-molecule analysis. Figure 2b is a plot of pore diameter versus electron-beam exposure time for over 50 nanopores formed in 45 ± 5-nm-thick Al_2O_3 membranes. Three stages were identified during nanopore formation, I, pore nucleation, II, rapid expansion, and III, controlled growth. A critical beam current density in excess of 2.6×10^6 A m^{-2} was required for nanopore nucleation in these membranes, as shown in Figure 2b. This is in good agreement with threshold current densities extracted by Salisbury et al. in experiments involving electron-beam-sputtered anodized alumina.[13] Below this threshold, topographical damage corresponding to the cleaving of Al—O bonds (bond dissociation energy of 513 kJ mol^{-1})[14] was observed but electron momentum was insufficient to induce an embryonic nanopore structure. Pore contraction mechanisms were also seen to dominate at low beam current densities, possibly due to surface-tension-driven oxide reflow, generation/recombination of closely spaced Frenkel pairs,[15] and mass transport of mobile atoms into the nucleation site. This is consistent with the "nanopore shrinking" phenomenon observed previously in SiO_2[9,16] and Al_2O_3 systems.[10] Two distinct sputter rates were observed during pore formation (stages II and III of Figure 2b) at current densities in excess of the threshold. The sputter rate transition observed cannot be attributed purely to the radial tapering in probe intensity as seen in Figure 2a. Intensity profiles of the probe reveal a differentiable Gaussian–Lorentzian function with no abrupt discontinuities, which in turn should translate to a gradual tapering in nanopore size with increasing electron-beam exposure, unlike the sudden rate transition observed in these experiments. Thus, an additional mechanism is expected to contribute to the material removal process in Al_2O_3. We attribute this result to electron-beam-induced crystallization coupled with direct metallization of the nanopore region.

2.3. Electron-Beam-Induced Crystallization

2.3.1. Electron Diffraction

NED was used to understand the structural phase transformation of the membrane material around the pore. Figure 3 shows the evolution of the structure of the amorphous membrane during the

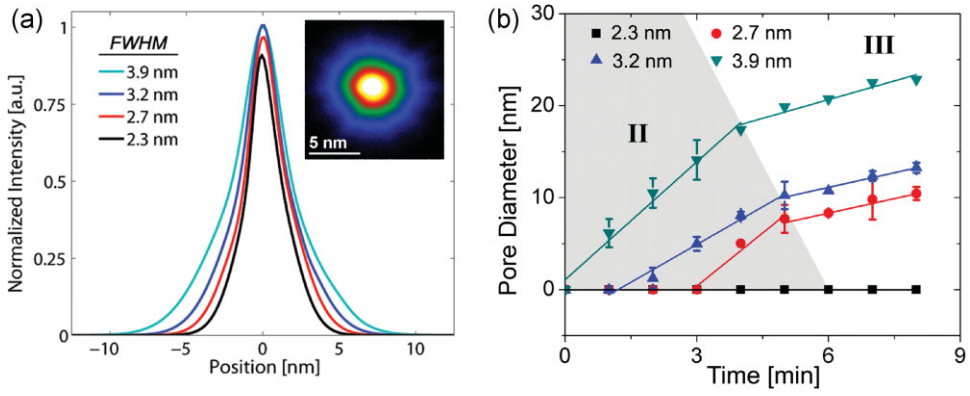

Figure 2. a) Intensity profiles of the focused electron probes used during nanopore formation constructed from TEM images. Intensity is normalized with respect to peak intensity of the 3.9-nm FWHM probe. Inset) TEM image of a 3.2-nm probe showing spatial intensity distribution. b) Nanopore sputtering kinetics illustrating pore diameter versus time for the various probes examined. Distinct expansion rates were observed delineating the three stages of pore formation, I) pore nucleation (not shown), II) rapid expansion, and III) controlled growth.

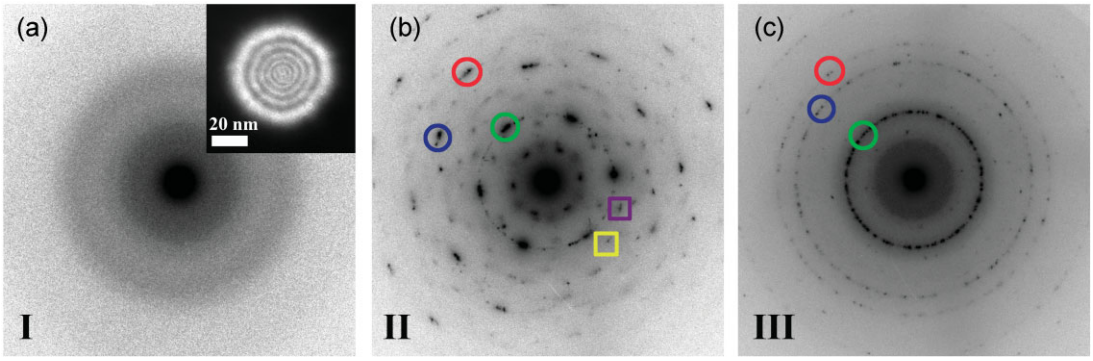

Figure 3. NED images taken using a ≈50-nm parallel electron probe as shown in the inset. a) NED image of the Al_2O_3 support prior to pore formation shows that the membrane is amorphous. b) NED pattern obtained by placing parallel electron probe over pore located in stage II of Figure 2b. Distinct spot reflections marked with circles are observed corresponding to the formation of γ- and α-Al_2O_3 nanocrystallites. Additional reflections marked by squares are from δ- and κ-phases. c) NED pattern obtained by placing parallel electron probe over pore located in stage III of Figure 2b. Continuous rings are observed, confirming that a polycrystalline material with preferred phases (γ and α) is formed by prolonged exposure to the convergent beam.

three stages of pore formation. Figure 3a shows a NED pattern from the amorphous membrane prior to exposure to the intense convergent electron beam. The inset shows the 50-nm coherent parallel electron probe with probe intensity set sufficiently low as to not alter the morphology of the nanopore. Beam current density in NED mode was $\approx 5.4 \times 10^3$ A m^{-2}, more than three orders of magnitude less than in convergent beam mode. The presence of diffuse rings and the absence of distinct rings or discrete spot reflections in Figure 3a confirms the lack of crystalline phase in the amorphous alumina membrane. Figure 3b shows an indexed NED pattern from a 14-nm pore formed after three minutes of sputtering with a 3.9-nm convergent electron probe. The NED pattern is typical of pore formation in stage II of Figure 2b. Discrete spot reflections of α- and/or γ-phase Al_2O_3 are visible, confirming the formation of nanocrystalline clusters of preferred phases. Reflection 1 (marked by green circle) exhibits sixfold symmetry and a *d*-spacing of 1.16 Å, which is indicative of either α- or γ-Al_2O_3. Reflections 2 (marked by blue circle) and 3 (marked by red circle) have *d*-spacings of 0.67 Å and 0.58 Å, respectively, which again matches both α- and γ-phase Al_2O_3. In α-Al_2O_3, Al^{3+} cations are octahedrally co-ordinated with average Al—O bond lengths of 1.92 Å.[17] γ-Al_2O_3 typically exhibits a cubic defect spinel-type structure with average Al—O bond lengths of 1.89 Å.[18] Reflections 4 and 5 (marked with squares) were significantly weaker and correspond to the nucleation of δ- and/or κ-phase nanocrystallites. The presence of multiple heterogeneous phases with varying bond lengths and co-ordinations indicates that an irregular density of exposed Al—O groups exist at the pore surface, which in turn corresponds to an irregular surface-charge distribution in a hydrated nanopore. This irregular charge distribution is expected to strongly impact DNA translocation kinetics. The diffraction pattern of Figure 3b confirms that initial electron-beam exposure to the amorphous material nucleates several crystal phases.

Figure 3c is a NED pattern from a 22-nm pore formed after eight minutes of sputtering using a 3.9-nm probe (stage III in Figure 2b). The NED pattern shows that prolonged exposure to the convergent beam results in a polycrystalline structure with preferred α- and/ or γ-phases. A comparison to Figure 3b shows that initial

electron-beam irradiation nucleates large, multiphase crystals indicated by the many discrete reflections of different *d*-spacings in Figure 3b. Prolonged exposure, however, generates many smaller crystals of preferred phase, indicated by polycrystalline rings with distinct yet fewer *d*-spacings (Figure 3c). These results provide evidence that the surface charge at the pore can be engineered based on critical electron doses. It is important to note that surface-charge density in this case is dependent on both the coordination of the phases and the pore size, which are not independent of each other. Therefore, only certain surface charge densities are likely possible. Surprisingly, there are no strong reflections corresponding to elemental Al in the NED patterns of stage II or III. Metallic Al would be expected as O is preferentially sputtered during prolonged electron-beam irradiation.

2.3.2. Electron Energy Loss Spectroscopy

EELS analysis provided further insight into the mechanisms driving pore formation and nanocrystallite nucleation. Figure 4 shows low-loss (plasmon) and core-loss EELS spectra taken before pore formation and after stage III of pore formation. Figure 4a shows the evolution of the low-loss region of the spectrum with prolonged electron-beam irradiation. Before exposure to the focused convergent electron beam, there is a broad, nearly symmetric plasmon peak located at ≈24 eV that corresponds to the bulk Al_2O_3 plasmon excitation. The plasmon peak measures longitudinal wavelike scattering of incident-beam electrons by delocalized valence electrons in the specimen and is sensitive to specimen bonding and thickness. Thicker specimens exhibit a taller plasmon peak due to a higher scattering probability. After pore formation via electron-beam-induced sputtering, the plasmon peak at ≈24 eV decays significantly and a secondary peak at ≈15 eV is formed. The total area under the low-loss spectrum decreases due to material removal at the pore nucleation site, resulting in fewer scattering events. The formation of this plasmon peak at ≈15 eV corresponds to plasmon excitations in metallic Al. Comparison to references shows no Al oxides have plasmon peaks at 15 eV.[19] This result confirms that Al-rich regions are formed at and near the pore edge due to the preferential desorption of O.

To confirm the presence of Al-rich nanocrystals, core-loss edge EELS was acquired before and after pore formation, as shown in Figure 4b. Prior to pore formation, the Al $L_{2,3}$ edge exhibits a sharp L_3 peak at 75 eV while the L_2 peak appears as a small shoulder (shown by i). Following the edge, there is a broad peak located at 99 eV. This is consistent with Al L edges acquired from amorphous Al_2O_3.[18] After pore formation, the $L_{2,3}$ edge appears more intense, indicating that there are more unoccupied states in the Al 3d band. In addition, the Al $L_{2,3}$ edge is chemically shifted to 72 eV and the L_3/L_2 splitting is more distinct with both edges displaying similar intensity (shown by ii). The post edge is rounder and the magnitude of the slope is greater. A comparison of the post edge to references shows that the EELS spectrum after pore formation is a linear combination of spectra acquired from metallic Al and γ-Al_2O_3.[12,18] Berger et al. obtained similar EELS spectra during the formation of trenches and slots in amorphous Al_2O_3 and Na-β Al_2O_3 systems.[12] The O K edge located at 537 eV did not change significantly after sputtering the pore, as seen in Figure 4c. Compositional variations were calculated by the k-factor[20] method and revealed that the O to Al ratio in the local nanopore region decreased from 1.5 before pore formation to ≈0.6 after pore formation. This result confirms that the sputtering process preferentially desorbs oxygen, leaving behind Al-rich nanocrystals resulting in a partially metallized nanopore. Similar phenomena were observed in electron-beam hole-drilling experiments conducted in Na-β Al_2O_3.[20] Coupled with studies by Berger et al. demonstrating the formation of continuous Al regions and "plugs" in electron-beam-irradiated metal β-aluminas,[12] in theory it should be possible to form a single nanoscale metallic contact within the nanopore using the method outlined in this work. Interfacing with electrodes patterned using electron-beam lithography techniques is also possible by rastering the focused electron probe over regions adjacent to and overlapping the metal contacts and the pore. A nanopore with an embedded electrode could be used to manipulate electric-field gradients in the pore and actively modulate surface charge and pore conductivity. Simulation work by Lagerqvist et al. demonstrated the ability to achieve single-nucleotide resolution by employing a nanopore sensor with embedded transverse sensing electrodes, with potential application to nanopore-based DNA sequencing.[11] With further characterization, the nanoscale metallization process reported here could help enable the possible realization of such a structure.

2.4. Nanopore Expansion Kinetics

The morphological transition of the pore from amorphous Al_2O_3 to a heterophase, Al-rich structure as confirmed through NED and

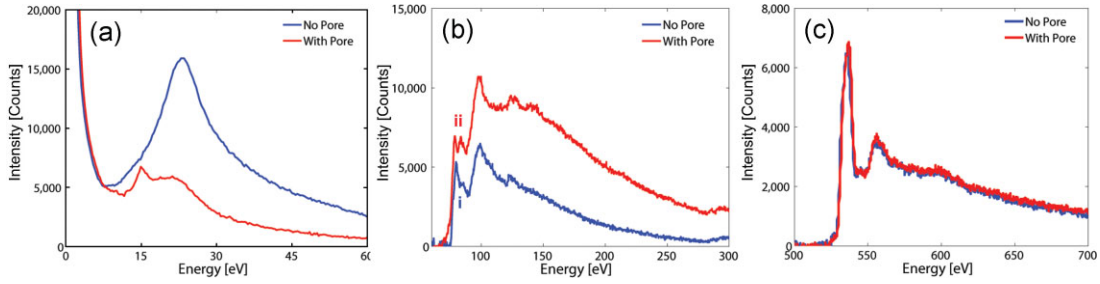

Figure 4. EELS spectra before (blue) and after (red) pore formation. a) Low-loss region shows attenuation of alumina plasmon peak located at ≈24 eV and the formation of a sharp peak at ≈15 eV corresponding to the bulk Al Plasmon. b) Background subtracted Al L-edge. Prior to pore formation, the Al L-edge resembles that of Al in Al_2O_3 form. i) Al $L_{2,3}$ edge. Post sputtering, the Al L edge consists of the superposition of L edges from metallic Al and Al in Al_2O_3 form. ii) Splitting of the Al $L_{2,3}$ edge. Results confirm the formation of metallic Al in the pore region. c) Background-subtracted O K-edge. O to Al ratio in the pore region is reduced from 1.5 to ≈0.6 due to preferential sputtering of oxygen.

EELS in turn affects subsequent pore expansion kinetics. Amorphous Al_2O_3 is sputtered primarily via volume-dissociated mechanisms exhibiting rapid and abrupt mass loss, attributed to the displacement of metallic Al and the formation of oxygen gas bubbles due to anion aggregation.[21,22] This mechanism explains the rapid pore expansion initially observed (stage II of Figure 2b). With continued electron-beam irradiation, the amorphous Al_2O_3 support transitions into a hybrid polycrystalline metallic structure (O to Al ratio of ≈0.6). Mass loss in this Al-rich, polycrystalline system (stage III of Figure 2b) is consistent with the Coulomb explosion displacement of atoms in Na-β Al_2O_3 systems. These hybrid systems are typically sputtered through surface-dissociated sputter mechanisms characterized by steady and continuous loss of material from the surface, resulting in lower sputter rates, Al aggregation, and the absence of O_2 bubble formation.[12,21] The decreased yet constant expansion rate observed in stage III of Figure 2b is consistent with this result. Mochel et al. also reported steady, constant growth rates during the formation of nanometer-sized holes in metal β-aluminas.[23] The absence of a sharp pre-peak at ≈532 eV in the O K edge spectrum of Figure 4c furthermore confirms that O_2 bubble formation and volume-dissociated mechanisms are less dominant in stage III. These results provide further insight into the lithographic properties of self-developing materials such as metal halides and metal oxides and are applicable to the rapid development of high-precision nanopore arrays in these material systems for the detection of ssDNA, dsDNA, RNA, and small proteins.

2.5. Surface-Enhanced DNA Detection

Surface-enhanced DNA detection was characterized through electronic measurements. DNA translocation experiments involved the electrophoretic transport of 5 kbp dsDNA through 7-nm-diameter nanocrystalline Al_2O_3 nanopores at voltages of 100 mV, 300 mV, and 500 mV, as shown in Figures 5a, b, and,c, respectively. Figure 5 illustrates characteristic current blockades observed at each voltage during DNA translocation. The insets of Figure 5 illustrate the blockade-free open-pore current at each voltage prior to the introduction of dsDNA. Table 1 summarizes experimental results including open pore current, I, average dwell times, $\mu(t_D)$, t_1 and t_2 timescales associated with translocation, average blockage ratios, $\mu(B_r)$, total number of events, n, and capture rates, R, at these respective voltages (see Table 1 for definitions of these terms). The results clearly indicate that average dwell times decrease with increasing voltage. As expected, an increase in the applied voltage results in an increase in the electrophoretic driving force experienced by the DNA molecule during transit, resulting in higher translocation velocities and shorter dwell times. This voltage-dependent behavior has been independently observed in biological α-hemolysin nanopores[24] and Si_3N_4[6] systems and serves as a complementary method to gel electrophoresis to verify DNA transport through nanometer-sized pores. A threshold voltage of 70 mV was observed in translocation experiments below which current blockades were not observed, suggesting the presence of a significant activation/entropic barrier associated with dsDNA transport through nanopores formed in Al_2O_3 membranes. In addition, biomolecule flux, n, and capture rate, R, increased exponentially with increasing voltage. Brun et al. also observed exponential increases in capture rate with increasing voltage during the transport of small polyelectrolytes through proteinaceous pores with capture rates following a simple Van't Hoff–Arrhenius relationship.[25] Similar trends were observed in experiments involving ssDNA passage through α-hemolysin.[26,27] Interestingly, mean dwell times at an applied bias of 100 mV yielded a translocation velocity of ≈ 1.4 nucleotides/μs, more than an order of magnitude slower than dsDNA translocation through Si_3N_4 nanopores (≈30 nucleotides/μs) at similar biases,[28] but an order of magnitude faster than ssDNA translocation through α-hemolysin.[6] Lubensky et al. accredited the slow translocation rates in α-hemolysin to strong polymer interactions with the pore

Table 1. Summary of results involving electrical sensing of 5 kbp dsDNA through a 7-nm nanopore at voltages of 100 mV, 300 mV, and 500 mV. t_D: Dwell time (time biomolecule resides in the pore). B_r: Blockage ratio (percentage of open-pore current that is blocked during DNA translocation). n: Biomolecule flux (total number of events during 5 minutes of recording). R: Capture rate (average number of translocation events per second).

V [mV]	100	300	500
I (open pore) [nA]	0.23	0.7	1.2
$\mu(t_D)$ [ms]	3.5 ± 10.8	1.3 ± 4.3	0.8 ± 1.9
t_1 [ms]	0.48 ± 0.05	0.35 ± 0.01	0.28 ± 0.02
t_2 [ms]	2.0 ± 0.7	2.9 ± 1.3	2.6 ± 2.2
$\mu(B_r)$ [%]	0.42	0.32	0.28
n [events]	1421	1954	5351
R [Hz]	4.7	6.5	17.9

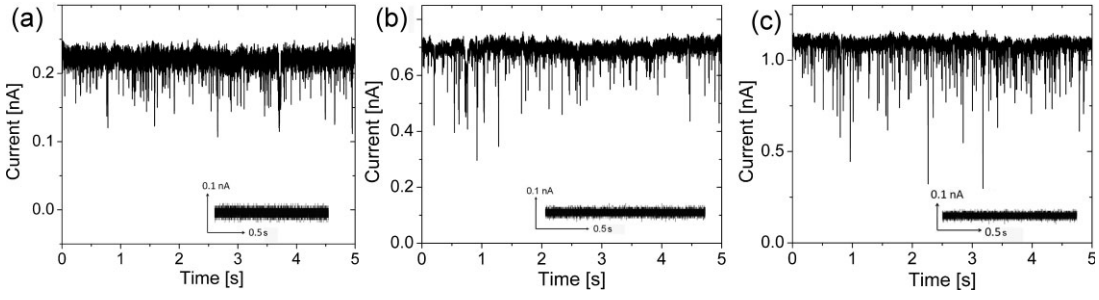

Figure 5. Typical current traces from a ≈7-nm nanocrystalline Al_2O_3 pore after the addition of 5 kbp dsDNA at a concentration of 6 nM to the *cis* side (anode) of the setup at applied voltages of a) 100 mV, b) 300 mV, c) 500 mV. Distinct downward current blockades were observed. Insets) Negative controls at each voltage; pore current is steady prior to the introduction of dsDNA. No blockades were seen.

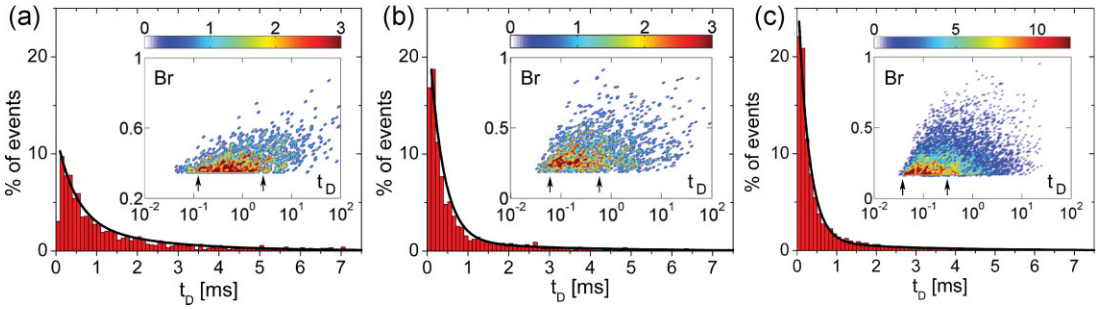

Figure 6. Dwell-time histograms at applied voltages of a) 100 mV, b) 300 mV, c) 500 mV. Each distribution is fitted with a bi-exponential function (black line) with two time constants, t_1 and t_2, indicating the two types of polymer transport, fast translocation governed by polymer hydrodynamics and slow translocation regulated by polymer–pore interactions. Insets) Blockage ratio B_r versus dwell time t_D (ms) at these respective voltages. Color bar represents number of events. At higher voltages, a greater percentage of events exhibit fast translocation dynamics bounded by the arrows in the insets. Translocation events exhibit clear voltage dependence.

walls.[29] We theorize that DNA–pore interactions also play an important role in slowing the rate of DNA transport through nanocrystalline Al_2O_3 nanopores. To verify this, a more in-depth examination of the translocation kinetics through these solid-state nanopores is needed. Figure 6a–c represents dwell-time histograms at applied voltages of 100 mV, 300 mV, and 500 mV, respectively. The insets of Figure 6a–c are event density plots of blockage ratio (B_r) versus dwell time (t_D) at these applied voltages. The red regions represent high event densities corresponding to the most probable event characteristics in terms of blockage ratios and translocation times. The most probable translocation characteristics are bounded by the arrows in the insets.

The dwell-time histograms of Figure 6 exhibit broad biexponential tails fitted using two time constants, t_1 and t_2, as summarized in Table 1. The results suggest that there are two distinct timescales associated with DNA transport through 7-nm Al_2O_3 nanopores. The shorter timescale, t_1, is associated with fast polymer transport through the pore with minimal DNA–pore interactions. t_1 timescales exhibit strong voltage dependence, suggesting that these events are indeed due to polymer transport through the pore as opposed to rapid, diffusion-driven collisions without translocation.[30] Such fast translocations are probable in larger 7-nm pores via translocation through the central pore region where the effects of surface-binding sites and surface charge are significantly screened. Fast translocation events were not observed in smaller 5-nm Al_2O_3 nanopores, suggesting that pore size and Debye layer thickness indeed play an important role in regulating the velocity of DNA transport.[10] t_1 timescales are also significantly faster than the characteristic relaxation time or Zimm time of 5 kbp dsDNA in 100 mM salt. The Zimm time, t_z, is an upper bound on the time taken by a polymer to reach an entropically and sterically favored state and is given by $t_z \approx 0.4\eta R_g^3/k_BT$.[3] Given solvent viscosity, $\eta = 1$ mPa s and polymer radius of gyration, $R_g = \sqrt{2l_pL} \approx 0.4$ μm at a persistence length of $l_p = 50$ nm for dsDNA in 100 mM KCl buffer, we calculate $t_z \approx 7$ ms. As $t_1 \ll t_z$, polymers exhibit a rigid or "frozen" polymer configuration in the pore during t_1 translocation events and thus interact minimally with the pore walls. This rigid-rod-like behavior is consistent with modeling results by Berezhkovskii et al. that predict decreasing dwell times and narrower event distributions with increasing applied force for the transport of rod-like macromolecules through nanochannels.[31] To reach a configuration that permits such fast translocations, polymers likely undergo coil-stretch transitions prior to entering the pore. In a positively charged nanopores, as is the case here at pH 7.5 (isoelectric point of $Al_2O_3 \approx 9$),[32] the electro-osmotic flow (EOF) is oriented in the same direction as polymer translocation, resulting in an absorbing region around the nanopore comparable in size to R_g of the polymer. Within this absorbing region, the velocity gradient of the fluid is larger than the critical velocity gradient necessary for coil stretching.[33] Molecules entering this region undergo coil-stretch transitions that help to elongate the molecule and reduce the entropic barrier associated with translocation, thereby allowing for fast translocations. The fast translocation events observed in these experiments are consistent with timescales ($\mu(t_D) \approx 162$ μs) associated with the transport of 6557 bp dsDNA through much larger ≈10-nm SiO_2 nanopores.[3]

The longer time scale, t_2, is associated with DNA translocations involving significant interactions with the nanopore. We observed similar phenomena in small 5-nm Al_2O_3 nanopores, characterized by a monoexponential decay in dwell-time histograms with time constants consistent with t_2 timescales (1.97 ± 0.2 ms).[10] Polymer–pore interactions were also reported in small 2.7–5-nm Si_3N_4 nanpores.[30] The origins of these interactions are hydrophobic and/or electrostatic in nature and are dependent partially on the material properties of the pore (stoichiometry, morphology, and surface roughness). NED and EELS confirmed the formation of heterophase crystalline domains (in particular γ- and α-phases) of varying bond lengths and co-ordinations in the nanopore region, resulting in non-uniform distributions of exposed Al−O groups at the pore surface. In a hydrated nanopore, these surface sites react with adsorbed water to form protonated hydroxyl groups at pH 7.5, resulting in a net positive, non-homogeneous surface-charge density across the pore. The existence of crystalline domains of varying charge density is likely as α-Al_2O_3 and γ-Al_2O_3 both exhibit different points-of-zero-charge (PZCs), estimated at pH 9.1 and pH 8.5 in monovalent salt solution, respectively.[34,35] In addition, the zeta potentials of these materials measured in pH 7.5 electrolyte are ≈50 mV and ≈25 mV, respectively,[36,37] and thus these charged domains are expected to interact differently with anionic DNA. Alterations to pore stoichiometry due to the preferential desorption of O and the

aggregation of Al is also expected to result in a distribution of equilibrium constants (pK) for the protonizable chemical sites across the pore. The resulting electrostatic interactions/binding between the non-homogeneous, net positively charged nanopore surface and anionic DNA is one factor contributing to the *slow* translocation velocities observed in these experiments. Modeling results by Kejian et al. confirmed that polymer translocation velocities in a solid-state nanopore are heavily dependent on zeta potential and surface charge.[38] Furthermore, studies by Kim et al. on nanopores derivatized with aminopropyltriethoxysilane relied on electrostatic binding events between the positively charged aminated surface and the negatively charged DNA backbone to slow down DNA transport through the pore.[39]

The strong electrostatic binding observed in our experiments was not reported in SiO_2 and Si_3N_4, likely as these systems exhibit a net negatively charged surface at pH 7.5 resulting from the deprotonation of surface silanol groups.[40] Furthermore, a comparison of the surface charge density of Si_3N_4 and γ-Al_2O_3 surfaces at pH 7.5 (in monovalent salt solution at concentration 1×10^{-4} M) revealed a charge density that is approximately six times higher in γ-Al_2O_3 (50 mC m^{-2}) than in Si_3N_4 (8 mC m^{-2}) systems.[34,41] Thus, polymer–pore interactions involving electrostatic binding events are expected to be more prominent in Al_2O_3 nanopores. Hydrophobic interactions between DNA bases and the pore surface may also be prevalent in Al_2O_3 nanopore systems. Simulation work by Aksimentiev et al. reported on such phenomenon in Si_3N_4, resulting in biomolecule adhesion and even partial unzipping of dsDNA during transport, leading to increased dwell times in the pore.[42] Such interactions may be enhanced in Al_2O_3 systems as the material undergoes significant surface roughening during electron-beam irradiation, as seen through irregular faceting and thickness variations across the pore region, thereby increasing the surface area available for hydrophobic polymer–pore interactions. Electron-beam-induced surface roughening during hole formation is particularly prominent in α-Al_2O_3 systems.[43] Given the hydrophobic/electrostatic interaction mechanisms described here and the comparability of t_z and t_2 timescales, it is expected that t_2 translocation events likely involve surface-dependent polymer–pore interactions, resulting in polymer relaxation and conformational change during translocation. Such polymer translocation events may be modeled as a series of thermally activated barrier hops over small energy barriers of varying height as opposed to single barrier-crossing events.[30] Our results clearly suggest that Al_2O_3 nanopore sensors serve as highly functional platforms for single-molecule DNA analysis with the ability to regulate the rate of DNA transport through complex surface interactions.

An exciting prospect emerging from this work is the potential modification of nanocrystalline Al_2O_3 nanopores with various surface chemistries to further enhance the sensitivity and chemical specificity of these nanoscale sensors. Liquid-phase silane-based chemistries are well characterized on Al_2O_3 surfaces, forming high-density, mechanically stable, self-assembled monolayers (SAMs) and are commonly used to chemically modify anodic aluminum oxide (AAO) nanoporous arrays.[44–46] This functionalization strategy is also applicable to the chemical modification of individual nanocrystalline Al_2O_3 nanopore sensors. Prior to chemical modification, the partially metallized nanopore surface needs to be fully oxidized in an O_2 plasma. Preliminary studies on silanized ALD Al_2O_3 surfaces confirm the formation of stable SAMs, verified through X-ray photoelectron spectroscopy, contact angle, and fluorescence measurements (data not shown). Target-specific molecular recognition in functionalized nanopore systems is achieved through the subsequent attachment of specific recognition sequences or tethered receptors to the silanized nanopore surface. This procedure has been successfully implemented in functionalized AAO nanoporous arrays, a specific example being the electrical detection of DNA hybridization reactions using AAO templates containing immobilized ssDNA probes. Using cyclic voltammetry methods, the authors were able to detect impedance shifts upon probe hybridization with complementary target ssDNA present in the solution phase.[47] Functionalized AAO nanoporous templates have also been successfully applied in DNA separation, sorting, and sequence recognition applications.[48] These "bulk" ensemble average methods however lack the single-molecule sensitivity that is inherent to individual solid-state nanopores. Therefore, by combining the molecular specificity reported in functionalized AAO template studies with the single-molecule detection capabilities of single-nanocrystalline Al_2O_3 nanopore sensors, a new family of highly sensitive, chemically selective nanopore sensors can be developed and tailored for specific biosensing applications. In drug screening and medicine, such technologies would provide a means to study the label-free, real-time kinetic analysis of biomolecular interactions at the single-molecule level, including protein–protein, protein–DNA, and receptor–ligand interactions.

3. Conclusions

This work presents the development of nanocrystalline surface-enhanced Al_2O_3 nanopore sensors for high-throughput DNA analysis. Nanopore formation through electron-beam-based decompositional sputtering of amorphous Al_2O_3 transformed the local nanostructure and morphology of the pore from an amorphous, stoichiometric structure (O to Al ratio of 1.5) to a heterophase crystalline structure with O to Al ratio of $\approx$0.6. Preferential phase transformations from γ-, α-, κ-, and δ-Al_2O_3 to purely γ- and α-phases were observed with increasing electron dose. Dose-dependent control over phase transformations at the nanopore/fluid interface is highly desirable and provides a novel method to engineer surface charge in the nanopore. The evolving nanostructure of the pore also affected nanopore expansion kinetics; rapid, abrupt mass loss observed in the amorphous state and steady material removal in the polycrystalline/metallic state was attributed to transitions from volume- to surface-dissociated sputtering mechanisms. In addition, sputtering induced the direct metallization of the pore region, as confirmed with EELS and NED. This in-situ metallization process provides a potential means to create nanoscale metallic contacts in the pore region for manipulating surface charge and pore conductivity.

DNA transport studies revealed an order-of-magnitude reduction in translocation velocities ($\approx$1.4 nucleotides/μs) in comparison to Si_3N_4 and SiO_2 architectures, accredited to strong electrostatic binding events between anionic DNA and the positively charged nanopore surface. These complex surface interactions are enhanced in Al_2O_3 due to high surface-charge

density, the nucleation of α- and γ-Al_2O_3 nanocrystallites, and high surface roughness. The enhanced sensitivity and favorable surface characteristics of Al_2O_3 nanopore sensors suggest that this metal oxide platform may indeed prove to be a viable and functional alternative to conventional Si_3N_4- and SiO_2-based nanopore systems, ideal for the detection and analysis of ssDNA, dsDNA, RNA secondary structures, and small proteins. In addition, this technology is compatible with various chemical-modification techniques to further enhance sensitivity and impart selectivity to the nanopore. Such technologies may find use in drug screening and medical applications involving label-free, real-time kinetic analysis of biomolecular interactions at the single-molecule level. This nanoscale sensor may also serve as a useful tool in studying the mechanisms driving biological processes including DNA–protein interactions, enzyme activity, cell signaling and regulation using gated, selective ion channels, and RNA translation using nuclear membrane pores. Hence, this technology can find broad application in bionanotechnology.

4. Experimental

Nanopore Fabrication: The nanopore fabrication process starts with double-sided polished ⟨100⟩ silicon wafers from Silicon Quest International thinned down to a final thickness of 300 ± 10 μm. Wafers were piranha cleaned (1:1 H_2SO_4:H_2O_2) for 15 minutes prior to introduction into the ALD flow reactor (Cambridge NanoTech Inc) to remove organics and to promote the formation of reactive hydroxyl surface groups. ALD was used to deposit 700 Å of Al_2O_3 at an average deposition rate of 0.96 Å/cycle at a platen temperature of 300 °C using tetramethyl-aluminum (TMA) as the metal precursor and water vapor as the oxygen precursor. One reaction cycle consisted of 0.05 s pulse of TMA, followed by 10 s evacuation of the reactor, 0.05 s pulse of water vapor, followed by another 10 s reactor evacuation to remove gaseous byproducts, primarily CH_4 and any unreacted species. Next, low-stress silicon nitride was deposited (STS Mesc PECVD System) using a mixed-frequency recipe consisting of alternating high-frequency and low-frequency deposition steps using process gases of SiH_4 and NH_3 at flow rates of 40 sccm and 55 sccm, respectively, at a platen temperature of 300 °C. High-frequency (HF: 6 s at 13.56 MHz, platen power 20 W) and low-frequency (LF: 2 s at 380 kHz, platen power 60 W) deposition steps resulted in stacked tensile and compressively stressed layers. Process optimization resulted in the formation of 500-nm-thick low-stress SiN films. Optical lithography and reactive ion etching (RIE) using CF_4-based etchants were used to pattern 30-μm square windows in the SiN layer. By controlled over-etching in the RIE, the thickness of the exposed Al_2O_3 region was thinned to a final thickness of 45 ± 5 nm as confirmed through TEM cross sectioning. The RIE process was conducted at a power of 90 W and chamber pressure of 35 mT using CF_4 as the precursor at a flow rate of 60 sccm. An etch rate of 625 Å min^{-1} was characterized for this recipe. Next, lithography was used to pattern 30-μm square openings on the wafer backside, aligned with the openings on the front side using AZ9260 photoresist and a Quintel Q7000 IR Backside Mask Aligner. The patterned photoresist layer defined the mask for the following backside deep Si trench etch. 300-μm-deep, high-aspect-ratio (10:1) trenches were next formed on the wafer backside using the Bosch process (deep RIE tool). The etch step was conducted at a chamber pressure of 37 mT for 12 s and platen power of 12 W with SF_6 and O_2 flow rates of 130 sccm and 13 sccm, respectively, per cycle. C_4F_8 sidewall passivation followed the etch step and was done at a chamber pressure of 18 mT for 8 s at a flow rate of 78 sccm. 495 such etch/passivation cycles were required to etch completely through the 300-μm-thick Si handle layer and to stop on the Al_2O_3 membrane layer. Nanopores of varying diameter were formed in free-standing 45 ± 5-nm-thick Al_2O_3 membranes using a focused electron beam from a JEOL JEM2010F field-emission TEM operated at 197 kV in convergent beam electron diffraction (CBED) mode. High beam current densities resulted in decompositional sputtering of the Al_2O_3 membrane.

Electron Microscopy Techniques: Characterization of the membranes and pores was carried out in a JEOL JEM2010F field-emission TEM operated at 197 kV in parallel-beam TEM imaging, NED, and EELS modes. NED patterns were acquired using a 50-nm parallel probe with a divergence angle less than 0.05 mrad [49]. The electron probe covered part of the pore and part of the membrane. The beam current density in NED mode was kept low to avoid microstructural changes in the specimen. Current densities in NED mode were more than 3 orders of magnitude less than in CBED mode. The camera length calibration for the diffraction pattern was obtained by calibrating the *d*-spacings with a single-crystal Si ⟨110⟩ sample under the same microscope conditions. Beam current densities were calculated using the total electron current incident on the imaging screen measured using a picoammeter and then dividing by the cross-sectional area of the probe at FWHM. EELS spectra were acquired in TEM imaging mode with a Gatan Imaging Filter model 2001. The low-loss region and Al $L_{2,3}$ and O K core loss edges were acquired with a selected energy dispersion of 0.3 eV/channel, a spectrometer collection angle of greater than 100 mrad, and an energy resolution of ≈1.5 eV measured by the zero loss peak. The core-loss edges presented are background subtracted with a power law. The inelastic mean free paths of 197 keV electrons in Al_2O_3 and Al were ≈160 nm and ≈150 nm, respectively [50]. The thickness of the membrane was 45 ± 5 nm or ≈0.3 mean free path. As the specimen thickness is thin and unchanged over a large area, the k-factor method of calculating the composition by the ratio of the integrated areas under the background subtracted O K and Al $L_{2,3}$ edges was calculated without taking into account plural scattering. The k-factor method requires the use of a standard sample with known composition. The membrane composition was measured using X-ray photoelectron spectroscopy to be stoichiometric Al_2O_3.

DNA Sensing Experiments: Prior to fluidic measurements, nanopore chips were solvent cleaned with acetone/methanol/deionized water (Millipore 18.2 MΩ-cm). The nanopore chips were then piranha cleaned in 3:1 H_2SO_4:H_2O_2 for three minutes to remove organic contaminants and to render the surface hydrophilic. A polydimethylsiloxane (PDMS) gasket with an aperture was then aligned and bonded to the front side of the chip to form a gigaohm seal, thereby reducing fluidic leakage and improving electrical isolation between the reservoirs. A subsequent plasma treatment was done on the chip to enhance the hydrophilicity and wettability of the pore (O_2 plasma at 90 W for 1 minute). The treated pores were immediately mounted between two chambers of a Delrin flow cell, and 1 M KCl with 10 mM Tris-HCl, pH 7.5 was introduced into both reservoirs. Immediate wetting and ionic conduction through the pore was observed. The pH of the ionic solution was 7.5, adjusted using dilute KOH solution and aqueous H_2SO_4. The ionic solution was filtered using a 0.2-μm lure lock filter to remove any large-particulate contamination. Current was measured by placing newly chlorided Ag/AgCl electrodes in each reservoir with the nanopore forming the only electrical/fluidic connection between the two compartments of the flow cell. The entire setup was housed in a double Faraday cage with a dedicated low-noise ground connection mounted on a vibration isolation table. The current signal was measured using the Axopatch 200B low-noise current amplifier (Axon Instruments, USA) operated in resistive feedback mode with $\beta = 1$. Data was low-pass-filtered at 10 kHz using the built-in 8-pole Bessel filter. The output signal was sent to a Digidata 1440A data-acquisition module (Axon Instruments, USA) and was digitized at 200 kHz and recorded using pClamp 10.2 software. Open-pore current was recorded prior to the insertion of dsDNA. DNA translocation studies involved the use of 5 kbp dsDNA (NoLimits) from Fermantas Inc. with dsDNA being inserted into the *cis* chamber (chamber with anode) at a final concentration of 6 nM.

Acknowledgements

We thank the staff at Micro and Nanotechnology Lab, UIUC and Shankar Sivaramakrishnan, Sukru Yemenicioglu, UIUC for TEM assistance. Research for this manuscript was carried out in part in the Frederick

Seitz Materials Research Laboratory Central Facilities, University of Illinois, which is partially supported by the U.S. Department of Energy under grants DE-FG02-07ER46453 and DE-FG02-07ER46471. We acknowledge the funding from the National Institutes of Health through the NIH Roadmap for Medical Research Nanomedicine Development Center (PN2 EY 018230), NIH R21 EB007472 and from Argonne National Laboratory, DOE-BES Grant DE-AC02-06CH11357 (DMSE, Digital Synthesis FWP).

Received: November 11, 2009
Published online:

[1] S. M. Iqbal, D. Akin, R. Bashir, *Nat. Nanotechnol.* **2007**, *2*, 243.
[2] U. Mirsaidov, W. Timp, X. Zou, V. Dimitrov, K. Schulten, A. P. Feinberg, G. Timp, *Biophys. J.* **2009**, *96*, L32.
[3] A. J. Storm, C. Storm, J. Chen, H. Zandbergen, J.-F. Joanny, C. Dekker, *Nano Lett.* **2005**, *5*, 1193.
[4] R. M. M. Smeets, S. W. Kowalczyk, A. R. Hall, N. H. Dekker, C. Dekker, *Nano Lett.* **2008**, *9*, 3089.
[5] J. Clarke, H. C. Wu, L. Jayasinghe, A. Patel, S. Reid, H. Bayley, *Nat. Nanotechnol.* **2009**, *4*, 265.
[6] P. Chen, J. Gu, E. Brandin, Y.-R. Kim, Q. Wang, D. Branton, *Nano Lett.* **2004**, *4*, 2293.
[7] J. Li, D. Stein, C. McMullan, D. Branton, M. J. Aziz, J. A. Golovchenko, *Nature* **2001**, *412*, 166.
[8] M. W. M. J. Kim, D. C. Bell, A. Meller, *Adv. Mater.* **2006**, *18*, 3149.
[9] A. J. Storm, J. H. Chen, X. S. Ling, H. W. Zandbergen, C. Dekker, *Nat. Mater.* **2003**, *2*, 537.
[10] B. M. Venkatesan, B. Dorvel, S. Yemenicioglu, N. Watkins, I. Petrov, R. Bashir, *Adv. Mater.* **2009**, *21*, 2771.
[11] J. Lagerqvist, M. Zwolak, M. Di Ventra, *Nano Lett.* **2006**, *6*, 779.
[12] S. D. Berger, I. G. Salisbury, R. H. Milne, D. Imeson, C. J. Humphreys, *Philos. Mag. B* **1987**, *55*, 341.
[13] I. G. Salisbury, R. S. Timsit, S. D. Berger, C. J. Humphreys, *Appl. Phys. Lett.* **1984**, *45*, 1289.
[14] M. O'Keeffe, J. A. Stuart, *Inorg. Chem.* **2002**, *22*, 177.
[15] J. C. Pivin, *J. Mater. Sci.* **1983**, *18*, 1267.
[16] H. Chang, F. Kosari, G. Andreadakis, M. A. Alam, G. Vasmatzis, R. Bashir, *Nano Lett.* **2004**, *4*, 1551.
[17] A. J. Bourdillon, S. M. El-mashri, A. J. Forty, *Philos. Mag. A* **1984**, *49*, 341.
[18] D. Bouchet, C. Colliex, *Ultramicroscopy* **2003**, *96*, 139.
[19] I. Stará, D. Zeze, V. Matolín, J. Pavluch, B. Gruzza, *Appl. Surf. Sci.* **1997**, *115*, 46.
[20] R. F. Egerton, *Electron Energy-Loss Spectroscopy in the Electron Microscope*, Plenum, New York **1996**.
[21] G. S. Chen, C. B. Boothroyd, C. J. Humphreys, *Philos. Mag. A* **1998**, *78*, 491.
[22] M. S. M. Saifullah, K. Kurihara, C. J. Humphreys, *J. Vac. Sci. Technol. B* **2000**, *18*, 2737.
[23] M. E. Mochel, C. J. Humphreys, J. A. Eades, J. M. Mochel, A. M. Petford, *Appl. Phys. Lett.* **1983**, *42*, 392.
[24] A. Meller, L. Nivon, D. Branton, *Phys. Rev. Lett.* **2001**, *86*, 3435.
[25] L. Brun, M. Pastoriza-Gallego, G. Oukhaled, J. Mathe, L. Bacri, L. Auvray, J. Pelta, *Phys. Rev. Lett.* **2008**, *100*, 158302.
[26] A. Meller, D. Branton, *Electrophoresis* **2002**, *23*, 2583.
[27] J. Nakane, M. Akeson, A. Marziali, *Electrophoresis* **2002**, *23*, 2592.
[28] D. Fologea, J. Uplinger, B. Thomas, D. S. McNabb, J. Li, *Nano Lett.* **2005**, *5*, 1734.
[29] D. K. N. Lubensky, D. R. Nelson, *Biophys. J.* **1999**, *77*, 1824.
[30] M. Wanunu, J. Sutin, B. McNally, A. Chow, A. Meller, *Biophys. J.* **2008**, *95*, 4716.
[31] A. M. Berezhkovskii, I. V. Gopich, *Biophys. J.* **2003**, *84*, 787.
[32] P. Chen, T. Mitsui, D. B. Farmer, J. Golovchenko, R. G. Gordon, D. Branton, *Nano Lett.* **2004**, *4*, 1333.
[33] C. T. A. Wong, M. Muthukumar, *J. Chem. Phys.* **2007**, *126*, 164903.
[34] S. Alami-Younssi, A. Larbot, M. Persin, J. Sarrazin, L. Cot, *J. Membr. Sci.* **1995**, *102*, 123.
[35] S. Veeramasuneni, M. R. Yalamanchili, J. D. Miller, *J. Colloid Interface Sci.* **1996**, *184*, 594.
[36] P. Bowen, C. Carry, D. Luxembourg, H. Hofmann, *Powder Technol.* **2005**, *157*, 100.
[37] G. V. Franks, L. Meagher, *Colloids Surf. A* **2003**, *214*, 99.
[38] D. Kejian, S. Weimin, Z. Haiyan, P. Xianglei, H. Honggang, *Appl. Phys. Lett.* **2009**, *94*, 014101.
[39] Y.-R. Kim, J. Min, I.-H. Lee, S. Kim, A.-G. Kim, K. Kim, K. Namkoong, C. Ko, *Biosens. Bioelectron.* **2007**, *22*, 2926.
[40] D. P. Hoogerheide, S. Garaj, J. A. Golovchenko, *Phys. Rev. Lett.* **2009**, *102*, 256804.
[41] R. M. M. Smeets, U. F. Keyser, D. Krapf, M.-Y. Wu, N. H. Dekker, C. Dekker, *Nano Lett.* **2006**, *6*, 89.
[42] A. H. Aksimentiev, B. Jiunn, G. Timp, K. Schulten, *Biophys. J.* **2004**, *87*, 2086.
[43] J. E. Bonevich, L. D. Marks, *Ultramicroscopy* **1991**, *35*, 161.
[44] S. W. Lee, H. Shang, R. T. Haasch, V. Petrova, G. U. Lee, *Nanotechnology* **2005**, *16*, 1335.
[45] S. Penumetcha, R. Kona, J. Hardin, A. Molder, E. Steinle, *Sensors* **2007**, *7*, 2942.
[46] V. Szczepanski, I. Vlassiouk, S. Smirnov, *J. Membr. Sci.* **2006**, *281*, 587.
[47] I. Vlassiouk, P. Takmakov, S. Smirnov, *Langmuir* **2005**, *21*, 4776.
[48] I. Vlassiouk, A. Krasnoslobodtsev, S. Smirnov, M. Germann, *Langmuir* **2004**, *20*, 9913.
[49] M. Gao, J. M. Zuo, R. D. Twesten, I. Petrov, L. A. Nagahara, R. Zhang, *Appl. Phys. Lett.* **2003**, *82*, 2703.
[50] K. Iakoubovskii, K. Mitsuishi, Y. Nakayama, K. Furuya, *Phys. Rev. B* **2008**, *77*, 104102.